Lower-Troposphere Refractivity Bias in GPS Occultation Retrievals

C. O. Ao,[1] T. K. Meehan,[1] G. A. Hajj,[1] A. J. Mannucci[1], and G. Beyerle[2]

Abstract. Analysis of atmospheric occultation data from the GPS/MET experiment has revealed that the refractivity retrievals in the lower troposphere were systematically smaller than those obtained with numerical weather prediction models. It has been suggested that the bias was due to a combination of atmospheric multipath, critical refraction, and receiver tracking errors. In this paper, we show that a similar bias exists in the CHAMP and SAC-C data and describe the characteristics of the bias based on over 6700 soundings from October 2001. Retrievals obtained using the recently introduced canonical transform method are shown to markedly reduce the refractivity bias; however, a significant bias still remains below 2 km altitude. To better understand the underlying causes of the bias, we perform an end-to-end simulation study that incorporates full-wave signal propagation and realistic receiver tracking effects using an ensemble of atmospheric profiles. We find that atmospheric ducting effects often associated with the top of the planetary boundary layer (PBL) at 1–2 km altitude would cause retrieval errors at and below the PBL even in the absence of the receiver errors. Furthermore, current implementation of the receiver tracking algorithm based on an enhanced version of the phase-locked loop could introduce additional errors under the low signal-to-noise ratio (SNR) conditions that are often encountered in the lower troposphere. The latter problem is expected to be resolved in the near future through the adoption of open-loop tracking and the removal of the navigation modulation from the GPS signal.

1. Introduction

The Global Positioning System (GPS) consists of nominally 24 satellites that continuously transmit radio signals at frequencies 1.57542 GHz (L1) and 1.22760 GHz (L2). As the GPS satellites rise or set behind the Earth, the signals as measured by a receiver on a low-earth orbit (LEO) are directly affected by the Earth's ionosphere and atmosphere. These events, known as GPS occultations, provide active limb sounding measurements of the Earth's atmosphere, with the advantages of global coverage, high vertical resolution, and the capability to operate under all-weather conditions. First proposed in 1988 [*Yunck et al.*, 1988], the concept was successfully demonstrated in the GPS/MET (GPS Meteorology) mission in 1995 [*Ware et al.*, 1996]. The recently launched German satellite CHAMP (CHAllenging Minisatellite Payload) and Argentinian satellite SAC-C (Satelite de Aplicaciones Cientificas-C), both equipped with the BlackJack GPS receiver supplied by the Jet Propulsion Laboratory (JPL), have been collecting occultation data nearly continuously since mid-2001, with a combined throughput of about 400–500 soundings per day [*Wickert et al.*, 2001; *Hajj et al.*, 2002a].

Radio occultation measurements are sensitive to the index of refraction $n(\mathbf{r})$ of the atmosphere along the signal propagation path. The basic observables in the GPS occultation are the phase and amplitude of the carrier signals. Technical issues involved in the calibration of the data to remove clock biases and ionospheric effects are discussed elsewhere [*Hajj et al.*, 2002b]. The retrieval methodology generally relies on the conversion of the observables into ray bending angles and impact parameters, denoted respectively as α and a (Fig. 1). Under the assumption of spherical symmetry (namely $n(\mathbf{r}) = n(r)$), each ray is uniquely identified by its impact parameter. Moreover, the relation $\alpha(a)$ can be integrated using the Abel inversion formula to yield the radial index of refraction profile as follows [*Fjeldbo et al.*, 1971]

$$\ln n(r) = \frac{1}{\pi} \int_a^\infty da' \frac{\alpha(a')}{\sqrt{a'^2 - a^2}} \tag{1}$$

where $a = n(r)r$. Since n is typically close to 1 in the atmosphere, it is more convenient to use instead the refractivity $N(r) = (n-1) \times 10^6$. The refractivity represents the basic occultation retrieval quantity through which other atmospheric quantities such as temperature, specific humidity, etc., are determined [*Kursinski et al.*, 1997].

Analysis of the GPS/MET data has shown that the refractivity retrieved was on average smaller than that obtained using numerical weather prediction (NWP) models in the lower troposphere [*Rocken et al.*, 1997]. A negative bias in refractivity translates to atmospheric conditions that are warmer and/or drier than the NWP analyses. From the comparison of specific humidity, it has also been found that the NWP analyses yield significantly moister conditions than GPS/MET retrievals in the lower troposphere [*Kursinski and Hajj*, 2001]. Moreover, the bias was shown to be larger in the tropics, suggesting a possible correlation with

[1]Jet Propulsion Laboratory, California Institute of Technology, Pasadena, USA.

[2]GeoForschungsZentrum (GFZ), Potsdam, Germany.

Paper number .
0148-0227/02/$9.00

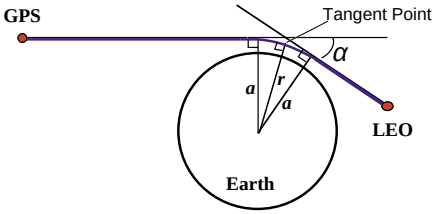

Figure 1. GPS occultation geometry.

water vapor abundance. A negative refractivity bias in the lower troposphere has also been reported recently for a small set of CHAMP and SAC-C data [*Wickert et al.*, 2001; *Ao et al.*, 2002; *Hajj et al.*, 2002b].

This so-called *negative N-bias* can be a result of retrieval error and/or NWP analyses error. If the N-bias reflects solely systematic errors in the NWP analyses, it serves to demonstrate the tremendous scientific value of GPS occultation data, especially for establishing unbiased long-term atmospheric climate records. On the other hand, if the N-bias reflects any error in the occultation retrievals, one needs to better identify existing problems in the retrieval process and find the corresponding solutions for correcting these problems. Retrieval error can arise from two distinct causes: (1) deficiencies in the inversion algorithm and (2) measurement errors introduced by the receiver.

In this paper, we aim to evaluate the impact of these two causes on the negative N-bias by using an end-to-end occultation simulation system developed at JPL. The focus of this study is on identifying possible sources of retrieval errors in the lower troposphere. The simulation system consists of a forward part that generates synthetic occultation data by propagating radio waves through a model atmosphere (specified by an input refractivity profile) and an inverse part that retrieves the refractivity profile. By directly comparing the retrieved profile with the input profile, retrieval errors can be easily assessed. The plan for the rest of this paper is as follows. In Sec. 2, the characteristics of the observed N-bias in current CHAMP and SAC-C occultation data are first discussed. The key components of the end-to-end simulation system and the simulation strategy are described in Sec. 3. In Sec. 4, the inversion methods are evaluated by examining the refractivity retrievals in the absence of receiver errors and noise. The effects of receiver errors on lower tropospheric retrievals are next considered in Sec. 5. In Sec. 6, we investigate how retrieval errors manifest in the N-bias by comparing the retrieved refractivity of the synthetic occultations with NWP profiles instead of the input profiles. Summary and conclusions are presented in Sec. 7.

A key assumption made throughout this work is that the atmosphere is spherically symmetric. This is justified more for its simplicity than its importance. When horizontal gradients in refractivity are significant, the idea of retrieving a single vertical profile from an occultation must be amended to account for the horizontal variations in the region. Moreover, the use of an inversion method which is based on a spherically symmetric atmosphere would introduce errors that need to be assessed. In spite of these considerations, it is of great value to first determine whether any N-bias could exist under the ideal condition of a spherically symmetric atmosphere where Abel inversion is supposed to be valid.

Since we are only concerned with lower tropospheric retrievals, we further assume that there is no ionosphere. Thus the simulation of only the L1 carrier signal is sufficient for the analysis here. Absorption in the neutral atmosphere is also neglected.

2. Characteristics of the N-Bias

In this work, we consider two different approaches of converting the occultation data into profiles of bending angle versus impact parameter $\alpha(a)$. The first has been used since the early days of planetary occultation experiments [*Fjeldbo et al.*, 1971; *Tyler*, 1987] and will be referred to as the "standard" (ST) method henceforth. ST relies entirely on the assumptions of geometric optics (GO) and single-ray propagation. In essence, the method deduces the arrival angle of the ray at the receiver based on the rate of change of the (accumulated) carrier phase. Knowing the positions and velocities of the transmitting and receiving satellites, one can then infer α and a simultaneously for each measurement. The advantage of ST is that it is algorithmically simple and efficient. However, it is not valid in the presence of atmospheric multipath, which occurs when multiple rays (with different values of α and a) arrive at a receiver location at the same time. In addition, by being a GO-based method, the vertical resolution of ST retrieval is limited by Fresnel diffraction to the first Fresnel diameter (~ 1 km) [*Kursinski et al.*, 1997].

The second approach is a "radioholographic" method known as the canonical transform (CT) method, which uses high-frequency wave theory to properly account for signal multipath and diffraction effects [*Gorbunov*, 2001, 2002]. Unlike ST, radioholographic methods such as CT use both the amplitude $A(t)$ and phase $\phi(t)$ to derive $\alpha(a)$ [for discussions of radioholographic methods other than CT, see *Gorbunov et al.*, 2000; *Igarashi et al.*, 2000; *Sokolovskiy*, 2000a]. Through an integral transform, the measurements of the complex field $\psi = A\exp(i\phi)$, which can be considered a function of the receiver positions, are combined to yield a reconstructed field $\Psi(a)$ which is a function of the impact parameter. The rate of change of the (accumulated) phase of the $\Psi(a)$ then gives the arrival angle of the ray directly as a function of impact parameter a. Provided that the a uniquely identifies a ray (true in the case of spherically symmetric atmosphere), CT completely resolves the multipath problem that plagues earlier methods. While ST is expected to perform substantially worse than CT in multipath regions, we include it in the present study since it is still the method most widely used in inverting occultation data. Comparisons between ST and CT retrievals also shed light on how unaccounted multipath effects show up in the N-bias.

A common way to assess the retrieved refractivity from an occultation is to compare it with global weather analyses such as those of the European Centre for Medium-Range Weather Forecasts (ECMWF) and the National Center for Environmental Prediction (NCEP). We consider the fractional refractivity difference defined as

$$\delta N(\text{occ}, \text{ana}) = (N_{\text{occ}} - N_{\text{ana}})/N_{\text{ana}} \qquad (2)$$

where N_{occ} is the refractivity profile retrieved from the occultation measurements and N_{ana} is the refractivity from the global analyses interpolated to the times and locations of the occultation tangent points. A statistical comparison can be made by averaging δN over a large number of occultations. Fig. 2 shows the zonal mean map of $\delta N(\text{occ}, \text{ECMWF})$ using occultation data from CHAMP and SAC-C in the month of October, 2001. A total of 6727 occultations are included in this comparison. The occultation profiles are sorted in latitude bins of 5° and altitude bins of 0.5 km.

The following characteristics of the N-bias can be noted:

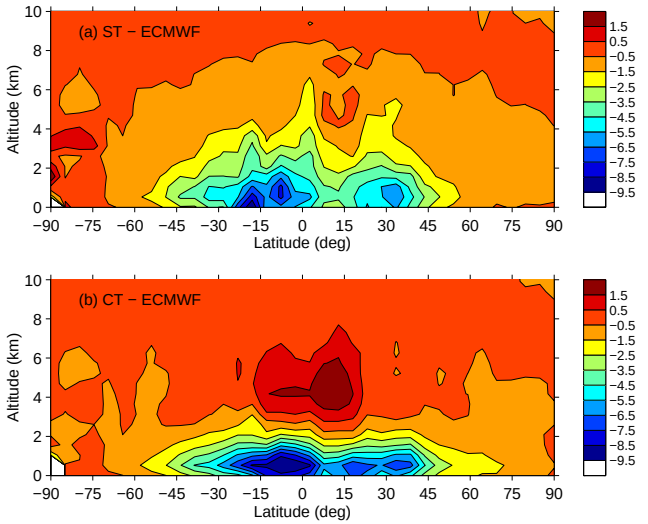

Figure 2. Fractional refractivity difference relative to ECMWF (%) based on the October, 2001 CHAMP and SAC-C data: (a) standard retrieval; (b) canonical transform retrieval.

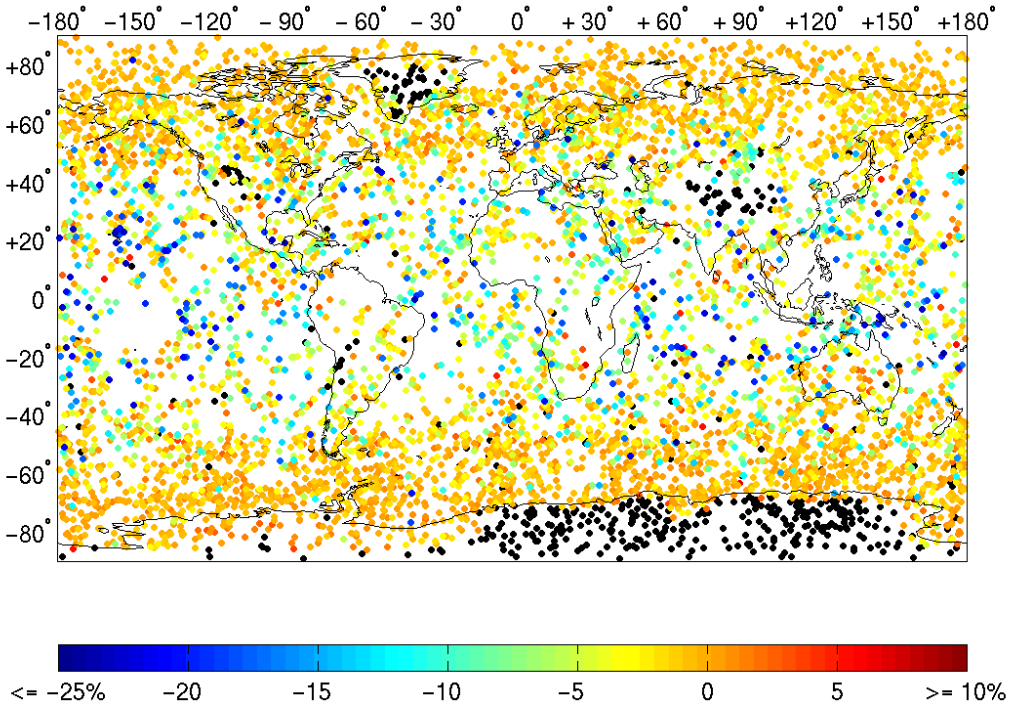

Figure 3. Fractional refractivity difference of the CT retrieval relative to ECMWF averaged over altitudes 0–2 km based on the October, 2001 CHAMP and SAC-C data. Occultations with their lowest tangent points above 2 km in altitude (mainly due to topography) are shown in black.

1. The negative bias is most severe in the tropics and at altitudes below 2 km. Near the surface, the bias can be as large as −10%. The peaks occur away from the equator and are stronger in the southern hemisphere.

2. The negative bias extends to mid-latitudes. For ST retrievals, the negative bias reaches up to 6 km in altitude.

3. CT reduces the negative bias from ST at altitudes above 2 km. In fact, a *positive* bias can be observed from 3–6 km in the tropics. A negative bias remains below 2 km and appears to peak near 1 km.

To investigate the global distribution of the N-bias, we average δN for each occultation over altitudes 0–2 km. The results corresponding to CT retrievals are shown in Fig. 3. Most of the occultations that show large negative bias take place over the tropical ocean. Fig. 4 further quantities the fact that the biased occultations are much more common in the tropics. However, it is important to note that there remains a significant number of occultations in the tropics with little or no bias. This suggests that the mean refractivity difference shown in Fig. 2 might be strongly influenced by a few strongly biased occultations. While some of the features shown in Figs. 2–4 are specific to the period of time considered here, the overall characteristics are representative of the N-bias in general.

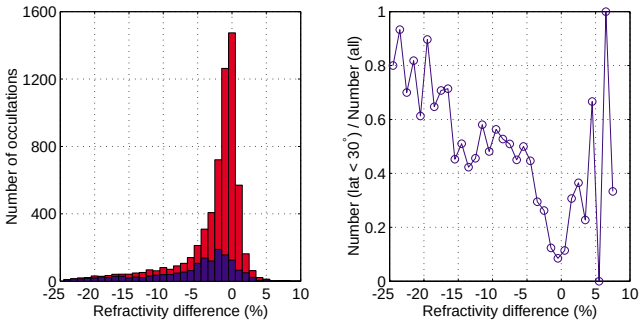

Figure 4. Histograms of fractional refractivity difference averaged over altitudes 0–2 km (*left*) and their ratio (*right*). Longer bars count all occultations in October, 2001. Shorter bars count only those with latitudes less than 30°.

We conclude this section by relating the refractivity difference to differences in temperature and water vapor. In the neutral atmosphere, the refractivity is related to the temperature T, pressure P, and water vapor pressure P_w as [*Smith and Weintraub*, 1953]

$$N = a_1 \frac{P}{T} + a_2 \frac{P_w}{T^2} \tag{3}$$

where

$$a_1 = 77.6 \text{ K mbar}^{-1} \quad \text{and} \quad a_2 = 3.73 \times 10^5 \text{ K}^2 \text{ mbar}^{-1}$$

Thus assuming near-surface atmospheric conditions of $P =$ 1000 mbar, $P_w = 30$ mbar, and $T = 300$ K, an N-bias of -5% translates into approximately $+10$ K in T or -5 mbar in P_w (holding other quantities fixed).

3. End-to-End Simulations

The source of the N-bias is difficult to identify because many factors could contribute to it. Ground truth data are not readily available, and errors in the analyses can be difficult to assess. To better understand and clarify the probable causes of the N-bias, we rely on end-to-end occultation simulations which allow us to compare the retrievals with the true profiles in a controlled setting and to isolate different factors that contribute to retrieval error. The key components of the simulator (Fig. 5) are described next.

3.1. Forward Propagator

Given a refractivity profile that describes the Earth's atmosphere, a forward simulator must be able to adequately

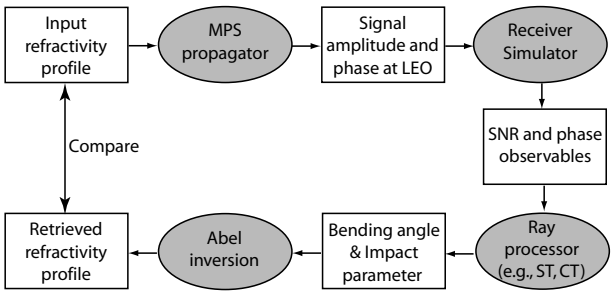

Figure 5. An end-to-end simulator for GPS occultations.

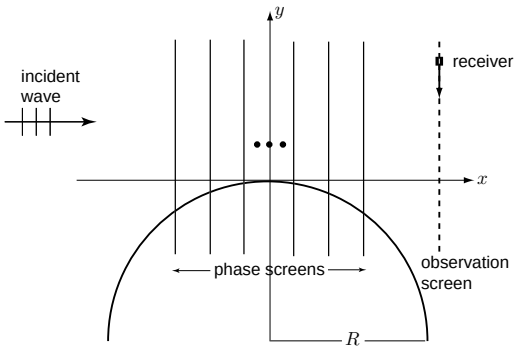

Figure 6. Geometry for the MPS forward propagator. The radius of the Earth R is set to 6370 km in the simulations.

model radio wave propagation transmitted through the atmosphere and accurately produce the wave field amplitude and phase at the receiver. Since atmospheric structures have scales much larger than the electromagnetic wavelengths of the GPS signal, the wave propagates predominately in the forward direction with little backscattering. In this case, the Helmholtz wave equation can be well approximated by the parabolic wave equation [*Martin*, 1992]. Thus the signal propagation for GPS occultation can be modeled efficiently with the multiple phase screen (MPS) method, which represents the Fourier split-step solution of the parabolic wave equation [*Levy*, 2000]. In this method, the atmosphere is approximated by a series of phase screens between which the signal propagates in vacuum. Unlike ray tracing, MPS includes full-wave diffraction effects and requires no special treatment for multipath. Its implementation in the context of GPS occultation has been well-documented [e.g., *Sokolovskiy*, 2001a].

The geometry for the MPS simulations is shown in Fig. 6. We use a total of 2000 phase screens with screen-to-screen separation of 1 km. Each screen consists of 2^{19} points with grid spacing of $\Delta y = 1$ m. For simplicity, we assume that the incident signal is a time-harmonic plane wave with L1 frequency ($f_{\text{L1}} = 1.57542$ GHz). The received amplitude and phase correspond to the complex field at $(x_{\text{obs}}, y_{\text{obs}})$, where $x_{\text{obs}} = 3000$ km and $y_{\text{obs}} = y_o - vt$, with v being the speed of the receiver and t is the observed time since the start of the occultation. Positive v corresponds to a *setting* occultation. We set $y_o = 60$ km, $v = 3$ km/s. Using these relations, the observed field amplitude $A(y_{\text{obs}})$ and phase $\phi(y_{\text{obs}})$ are converted into functions of time: $A(t)$ and $\phi(t)$. To mimic the 50 Hz processing of a real occultation, the MPS data within every $T = 20$ msec interval (corresponding to a spatial interval of 60 m in the observation plane) are averaged. The final products $\langle A(t_i) \rangle$ and $\langle \phi(t_i) \rangle$, with $t_i = (i-1)T$ $(i = 1, 2, 3, \ldots)$, are the final inputs to the receiver simulator. (The angular brackets $\langle\ \rangle$ will be dropped subsequently.)

3.2. Receiver Simulator

Real occultation data contain system noise and tracking errors, so these effects need to be properly included in the simulation system to ensure that the synthetic occultations are realistic. The algorithm used to simulate the tracking of GPS signal here is *essentially identical* to that currently employed by the BlackJack receiver onboard CHAMP and SAC-C. This corresponds to an enhanced version of the digital phase-locked loop (PLL) and is designed to track the

signal through an extended period of low SNR, a condition that often exists in the lower troposphere. A realistic receiver simulator is a crucial part of the analysis, without which we could not draw firm conclusions on the retrieval characteristics of the real occultations based on simulation results.

The actual GPS signal is a spread spectrum where the carrier signal is modulated using a bi-phase shift keying (BPSK) scheme [*Spilker*, 1996]. In particular, the C/A code changes the L1 carrier phase between 0 and π at a rate of 1.023 MHz. In addition, the signal is BPSK-modulated at a slower rate of 50 Hz for the encoding of the navigation messages. Thus the tracking of GPS signal requires both code and carrier tracking loops. For the sake of simplicity, we assume that the code modulation has already been stripped off. No significant difference is expected from this simplification. For an occultation simulation study in which the C/A code modulation is incorporated, the readers are referred to the recent work by *Beyerle et al.* [2002]. The data input to the receiver simulator are in the form of

$$u(t_i) = D(t_i)A(t_i)\exp(i\phi(t_i)) \tag{4}$$

where $D(t_i) = \pm 1$ are the 50 Hz navigation modulation.

In PLL, the data are obtained by correlating the complex signal with a predicted signal of the form $\exp(-i\phi_{\rm mod}(t))$, where $\phi_{\rm mod}$ is the tracking loop model phase which is computed based on the preceding phase measurements. The BlackJack receiver uses a third-order tracking loop that maintains and updates the phase $\phi_{\rm mod}$, the phase rate $\dot{\phi}_{\rm mod}$ (equivalently the Doppler frequency $f_{\rm mod} = \dot{\phi}_{\rm mod}/(2\pi)$), and the phase acceleration $\ddot{\phi}_{\rm mod}$. The receiver simulator computes the in-phase and quadrature correlation sums as follows

$$\begin{aligned} I_i &= \tau\left(\mathrm{SNR}_o\sigma\sqrt{T}\right)D(t_i)A(t_i)\cos[\phi(t_i)-\phi_{\rm mod}(t_i)] \\ &\quad +\sqrt{3}\sigma N_1 \end{aligned} \tag{5}$$

$$\begin{aligned} Q_i &= \tau\left(\mathrm{SNR}_o\sigma\sqrt{T}\right)D(t_i)A(t_i)\sin[\phi(t_i)-\phi_{\rm mod}(t_i)] \\ &\quad +\sqrt{3}\sigma N_2 \end{aligned} \tag{6}$$

where the first term on the right hand side represents the signal and the second term the noise. The various symbols are:

- SNR_o is the nominal (1-sec) voltage signal-to-noise ratio (SNR) in the absence of the atmosphere. For the simulations shown here, SNR_o is set to 600, which correspond approximately to the average value of the L1 signal for CHAMP and SAC-C [*Hajj et al.*, 2002a]. The free-space SNR per sampling interval is then $\mathrm{SNR}_o\sqrt{T}$, with T being the sampling interval in seconds.

- σ is the root-mean-square noise for the 1-bit sampled data per sampling interval T. For 50 Hz sampling with the BlackJack receiver, $\sigma \approx \sqrt{N_s T} \approx 700$, where $N_s \approx 26\times 10^6$ is the number of 1-bit samples per second. Note that the final results will not be affected by this parameter besides an overall scale factor. It is merely chosen this way so that the correlation sums provided to the tracking software will have the same order of magnitude as those coming from the actual GPS signal processing tracking hardware.

- N_1, N_2 are uniformly distributed random numbers from -1 to 1. The factor of $\sqrt{3}$ is needed to make σ the RMS value of the probability distribution.

- τ is an amplitude correlation factor that arises from the deviation of the measured Doppler frequency $f = \dot{\phi}/(2\pi)$ from tracking loop model [e.g., *Thomas*, 1995]:

$$\tau = \frac{\sin(\pi(f-f_{\rm mod})T)}{\pi(f-f_{\rm mod})T} \tag{7}$$

The occultation observables are extracted as follows:

$$A_{\rm rec}(t_i) = \sqrt{I_i^2+Q_i^2} \tag{8}$$

$$\phi_{\rm rec}(t_i) = \phi_{\rm mod}(t_i)+\phi_{\rm res}(t_i) \tag{9}$$

where the residual phase $\phi_{\rm res}$ is

$$\phi_{\rm res}(t_i) = \mathrm{atan}\left(\frac{Q_i}{I_i}\right) \tag{10}$$

The use of atan in extracting the residual phase restricts its values to $-\pi/2 \le \phi_{\rm res} \le \pi/2$ but allows us to ignore the overall sign of I_i and Q_i. Therefore, it is unaffected by the navigation data bit modulation $D(t_i)$. In actual occultation data, the amplitude is usually quoted in terms of the 1-sec SNR. Thus we scale the output amplitude ($A_{\rm rec}(t_i) \to A_{\rm rec}(t_i)/(\sigma\sqrt{T})$) such that $A_{\rm rec}(t_i) = \mathrm{SNR}_o$ in the absence of the atmosphere and noise.

The PLL effectively recovers the signal phase and amplitude as long as $\phi_{\rm mod}$ ($\dot{\phi}_{\rm mod}$) stays reasonably close to true ϕ ($\dot{\phi}$). However, the sharp refractivity structures that affect the retrievals in the lower troposphere also pose problems for the GPS receiver by dramatically decreasing the SNR (Sec. 4). Under such low SNR conditions, it is difficult for the tracking loop to maintain an accurate phase model for use in the PLL [e.g., *Sokolovskiy*, 2001b]. To handle this kind of situation, a special tracking scheme known as *flywheeling* (FW) has been implemented in CHAMP and SAC-C. The FW mode is triggered when the SNR drops below a predetermined threshold (~ 50). During FW, the receiver computes the phase model based on the extrapolation of previous phase measurements (~ 1 second of data) taken when the SNR is above the trigger threshold. This avoids the use of unreliable phase measurements in the tracking loop taken when SNR is low. FW can be expected to work reasonably well for a brief period of time after the trigger, when the extrapolated model phase does not stray too far off from the true phase. If, at a later time, the SNR rises above the threshold, the receiver will switch back to traditional PLL mode. The FW-enhanced PLL allows the GPS signal to be tracked through difficult periods of momentarily low SNR as it traverses the lower troposphere and enables occultation data to be continually collected down to the surface of the Earth.

3.3. Inversion

After the occultation data are processed by the receiver simulator, they are inverted to yield the refractivity profile. As described previously, the ST and CT methods first convert the observed amplitude and/or phase into bending angle versus impact parameter $\alpha(a)$. The Abel inversion formula Eq. (1) is then used to derive the refractivity profile. For ST, the carrier phase data within a Fresnel scale are smoothed to eliminate the diffraction effects [*Kursinski et al.*, 1997; *Hajj et al.*, 2002b]. To reduce the effects of system noise in the data, the phase of the CT field $\Psi(a)$ are smoothed in a similar way, but with a fixed spatial window of $\Delta a = 200$ m.

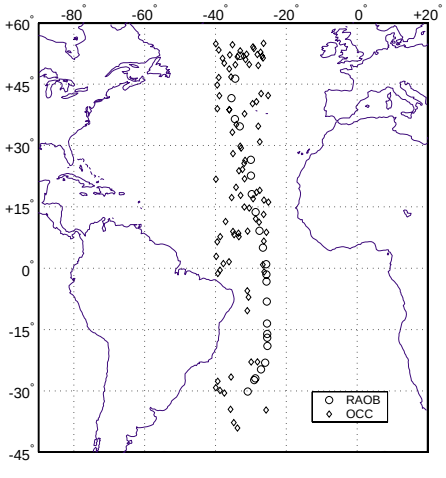

Figure 7. Locations of radiosonde observations (RAOB). Also displayed are the sounding locations of the CHAMP and SAC-C occultations (OCC) used in Sec. 6. The radiosonde observations and the occultations both occur in October but are separated by five years (1996 and 2001, respectively).

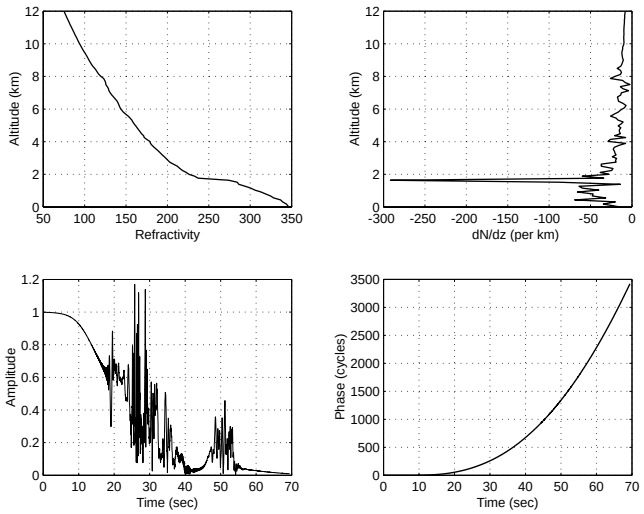

Figure 8. A simulated setting occultation. *Top*: Input refractivity and its gradient. *Bottom*: MPS-generated amplitude and phase.

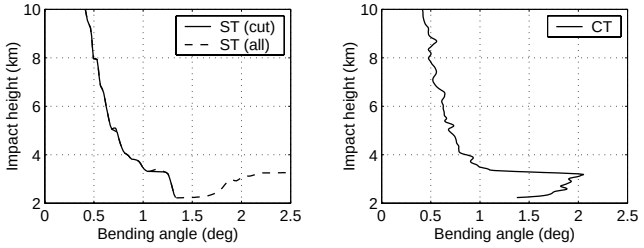

Figure 9. Bending angle profiles $\alpha(a)$ derived using ST and CT inversion. Impact height is defined as $a - R$, where R is the local radius of curvature of the Earth. ST infers multiple bending angles for a given a in multipath regions (*all*). The profile used in the Abel inversion (*cut*) has part of the data points removed so that it is forced to be single-valued.

3.4. Simulation Strategy

In order to capture a variety of atmospheric conditions, the simulations are performed using an ensemble of 24 refractivity profiles that are obtained from high-resolution radiosonde observations. These radiosonde measurements were taken over the Atlantic Ocean in October 1996 during the ALBATROS field campaign aboard the research vessel POLARSTERN. The locations of these observations are shown in Fig. 7. Being mostly over tropical ocean, a significant fraction of the simulated occultations is expected to exhibit a negative N-bias. The radiosonde profiles are available with 10–15 m vertical resolution in the lower troposphere. However, to prevent small-scale instrumental noise in the radiosonde data (mainly from the humidity sensor) from generating unphysically large amplitude and phase scintillations, a running-window average of 100 m width is applied to smooth the refractivity profiles. Since we are interested only in lower tropospheric retrievals, the refractivity profiles above 15 km are replaced by a simple exponentially decaying function of altitude.

4. Results with Perfect Receiver

We first consider the case where the receiver perfectly reproduces the signal amplitude and phase. In other words, the receiver simulator is taken out of the simulation chain (cf. Fig. 5); we shall also refer to the perfect receiver case as the case of "no receiver". This constitutes a test of the inversion methods. An example for one of the 24 simulated occultations (latitude 16.07°S, longitude 25.40°W) is shown in Fig. 8, along with the corresponding profiles of input refractivity and its gradient. The gross behavior of the amplitude and phase can be understood in simple terms. The smooth part of the refractivity profile acts as a diverging lens, which causes the ray to defocus and bend as it traverses the troposphere. In addition, small-scale structures in the refractivity profile cause the signal to interfere and diffract, leading to amplitude and phase scintillations. These effects are especially pronounced in the amplitude. In particular, it is interesting to note the strong refractivity gradient associated with the top of the planetary boundary layer (PBL) just below 2 km altitude causes the signal to nearly disappear for a few seconds near $t = 40$ sec. Similar "outages" are frequently observed in real occultation data [*Hajj et al.*, 2002a].

Applying the ST and CT methods on this occultation, we derive the bending angle profiles $\alpha(a)$ shown in Fig. 9. It can be seen (most obviously below the impact height of 3 km), that ST associates multiple bending angles with a given impact parameter. This is a clear violation of the laws of geometric optics when the atmosphere is spherically symmetric. The unphysical bending angle profile is a direct result of atmospheric multipath [*Gorbunov and Gurvich*, 1998], where ST misinterprets the phase rate by assuming that it is due to a single ray. Since Abel inversion requires that $\alpha(a)$ is single-valued, an *ad-hoc* procedure is usually adopted where a is forced to be a monotonously decreasing function of α by discarding part of the data. This procedure often results in bending angles that are smaller than the true values. In contrast, CT is capable of resolving the multipath ambiguities completely and rigorously, yielding a well-defined bending angle profile [*Gorbunov*, 2001, 2002].

Fig. 10 shows the retrieved refractivity profiles following Abel inversion of the bending angle profiles in Fig. 9. As expected, the truncated $\alpha(a)$ from ST results in a large negative error in refractivity, particularly below 2 km. CT gives a substantial improvement over ST. Nonetheless, it too results in negative refractivity errors below 2 km. Clearly, something other than multipath is responsible here.

It turns out that this error is caused by atmospheric ducting, where the refractivity gradient is so large that rays become internally reflected between atmospheric layers [*Hall*, 1979]:

$$\frac{d(nr)}{dr} < 0 \tag{11}$$

Taking $r = 6370$ km and $n \approx 1$, the ducting condition becomes $dN/dr < -157$ km^{-1}. A quick look at Fig. 8 confirms that the input refractivity gradient exceeds the critical value of -157 near the top of the PBL. When ducting occurs, rays within a certain range of tangent points will be trapped within the atmosphere and will not emerge to reach the receiver. Conversely, rays with any given impact parameter will never become tangential to the surface within these heights. Thus the existence of a ducting layer violates an implicit assumption used to derive the Abel inversion formula, i.e., that all heights in the atmosphere can be associated with a ray tangent point that relates to its impact parameter by the relation $n(r)r = a$.

The effect of ducting is illustrated in Fig. 11, where we plot the quantity nr as a function of r using the refractivity profile shown in Fig. 8. For $r \geq r_u$ or $r \leq r_l$, nr is monotonically decreasing with r and can be identified as the impact parameter. The top of the ducting layer $r = r_u$ corresponds to the local maximum where $d(nr)/dr = 0$. At this point, the impact parameter is $a_s = n(r_u)r_u$. The bottom of the ducting layer $r = r_l$ corresponds to the point below r_u where $n(r_l)r_l = a_s$. For $r_l < r < r_u$, the impact parameter in the sense of $a = n(r)r$ is ill-defined. However, $\alpha(a)$ is still well-defined for all values of a, except for a singularity at $a = a_s$, where α is formally infinite. Applying Abel inversion without realizing the existence of the ducting layer would yield a negatively biased refractivity profile below r_u with a gradient which is always less than the critical limit. This is the case even if we could manage to integrate over the bending angle singularity in a_s exactly. Thus atmospheric ducting represents a fundamental limitation of Abel inversion and affects both ST and CT retrievals. Fig. 11 shows that the retrieved refractivity is biased not only within the ducting layer but also well below it.

Ducting is a phenomenon which has been well-known among the radio science community. Most of the recent works are focused on *surface* ducts in marine environment (as opposed to the *elevated* ducts considered here), which greatly affects surface radar operations [e.g., *Anderson*, 1995; *Hacck and Burk*, 2001]. The impact of ducting on radio occultations has only begun to be appreciated. The effects described above are also clarified independently by *Sokolovskiy* [2002] (note that the term "super refraction" was used in that paper to describe ducting).

Fig. 12 shows the refractivity retrievals for all 24 simulated occultations. CT gives very accurate refractivity above 2 km. Below 2 km, ducting causes a range of negative errors that reach up to -8%. The errors decrease towards the surface and away from the ducting layer. On average, CT gives a mean negative N-bias which is within -1% (at about 1 km in altitude). For ST, significant negative bias exists up to 6 km in altitude, with a mean error exceeding -4% at the surface. Thus even though CT is not perfect, it represents a tremendous improvement over ST.

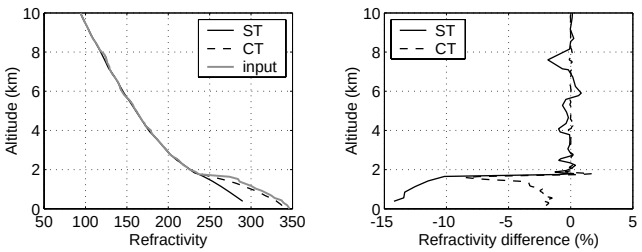

Figure 10. Refractivity retrievals after Abel inversion of the bending angle profiles in Fig. 9.

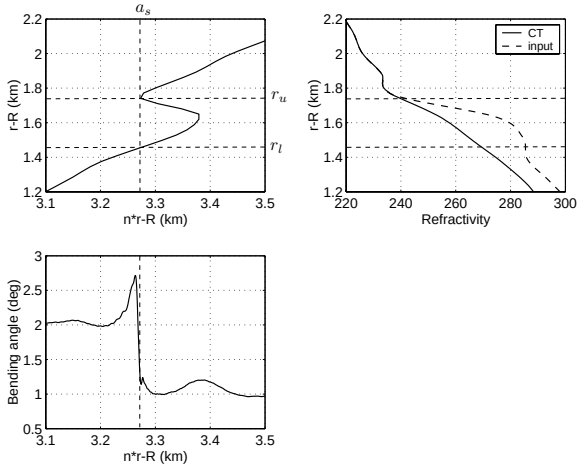

Figure 11. Illustration of how ducting affects the CT retrieval. In order to display the features near the ducting layer more clearly, a smaller smoothing interval of $\Delta a = 20$ m instead of 200 m is used here.

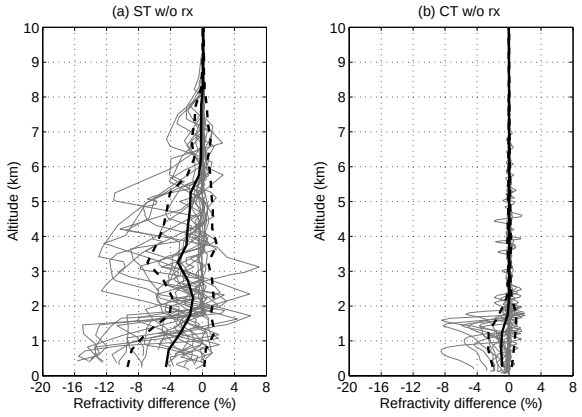

Figure 12. Fractional refractivity difference for all 24 occultations without receiver simulation. Thick solid line represents the mean. Dashed lines represent ± 1 standard deviation from the mean.

5. Results with Realistic Receiver

As evidenced in Fig. 8, strong defocusing and severe amplitude scintillation conditions often occurring in the lower troposphere cause the SNR to decrease dramatically and present challenging conditions for the receiver tracking the signal. In this section, we evaluate how the refractivity retrievals are affected by the presence of tracking errors.

Fig. 13 shows the signal amplitude $A_{\rm rec}$ for the occultation in Fig. 8 after the MPS data are processed by the receiver in the manner described in Sec. 3.2. For comparison, the input amplitude is also shown ("w/o rx") but is scaled by a constant factor of $\mathrm{SNR_o} = 600$ (i.e., $A{\cdot}\mathrm{SNR_o}$). The tracking performance can be viewed in terms of the amplitude error ($A_{\rm rec} - A \cdot \mathrm{SNR_o}$), the phase error ($\Delta\phi = \phi_{\rm rec} - \phi$), and the frequency error ($\Delta\dot{\phi}/(2\pi)$).

In general, we can identify three separate "tracking regions" in the data:

I. SNR remains larger than the FW threshold of 50. FW is never engaged ($t \lesssim 25$ in Fig. 13). Phase is accurately reproduced.

II. The receiver frequently switches between FW on and off modes as the SNR fluctuates about the FW threshold ($25 \lesssim t \lesssim 55$ in Fig. 13).

III. SNR remains below the threshold throughout. FW is always engaged ($t \gtrsim 55$ in Fig. 13). Recovered phase tends to drift off from the true value as time goes on.

Fig. 14 shows the refractivity retrieval results for this occultation when the effects of system noise and receiver tracking errors are included. Comparison with the refractivity retrievals without receiver errors ($\delta N(\mathrm{rx, no\ rx})$) shows that the tracking errors manifest themselves in different ways depending on the inversion methods, especially in the altitude range between 2 and 6 km. Below 2 km, the negative refractivity errors increase for both ST and CT retrievals.

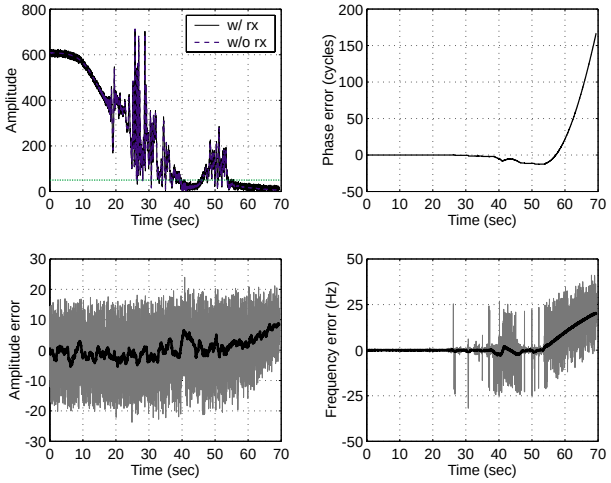

Figure 13. Receiver tracking results for the simulated amplitude and phase shown in Fig. 8. The thick black lines in the amplitude and frequency errors represent 0.5-sec averaging of the data.

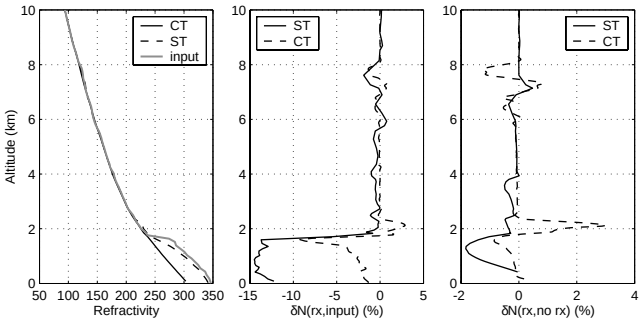

Figure 14. Refractivity retrievals with receiver errors and noise added.

The retrievals for all 24 simulated occultations are shown in Fig. 15. Relative to the retrievals without receiver errors (cf. Fig. 12), the mean N-biases below 2 km are now substantially increased for both ST and CT. However, it is clear, particularly for CT, that the increase in mean bias is largely caused by a few strongly biased retrievals. The mean bias will be much reduced if we discard these "outliers". Disregarding the outliers, we find that the CT retrieval errors below 2 km with and without receiver simulations are loosely correlated. The refractivity errors with realistic receiver are roughly 50% larger than the refractivity errors with perfect receiver. The increase in negative bias is due to the underestimation of the large bending angle near the ducting singularity at a_s (cf. Fig. 11). On the other hand, above 2 km, the CT retrieval errors of $\approx \pm 2\%$ appear to be more random, with roughly equal occurrences of positive and negative errors. We examine tracking data in more detail below in order to gain a better understanding of the nature of the tracking errors and how they propagate in CT retrievals.

In contrast to ST, radioholographic methods such as CT use the complex signal $A_{\rm rec}(t)\exp(i\phi_{\rm rec}(t))$. Being an amplitude-weighted method, it is reasonable to expect that tracking region II, where the SNR is large enough for the

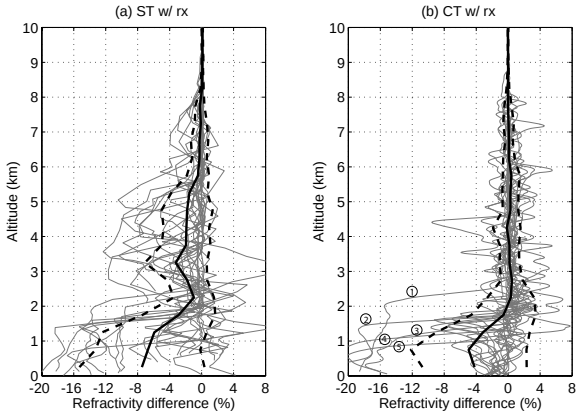

Figure 15. Fractional refractivity difference for all 24 occultations with receiver errors and system noise added. Thick solid line represents the mean. Dashed lines represent ±1 standard deviation from the mean. The "outliers" in the CT case are marked by numbered circles.

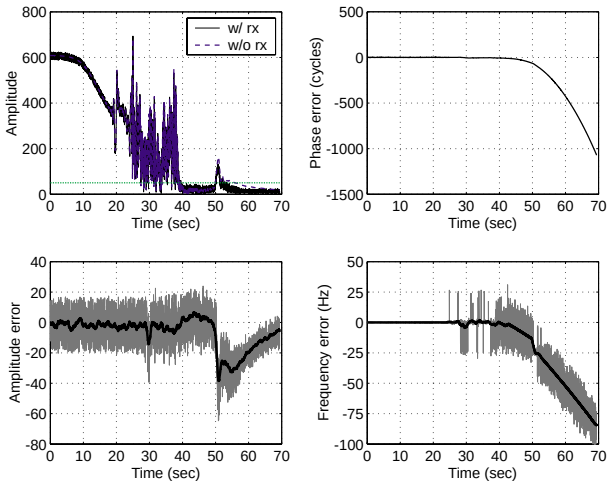

Figure 16. Tracking results for outliers No. 5 in Fig. 15.

tracking loop to switch FW off part of the time, has the most influence on CT retrieval in the lower troposphere. In particular, the CT outliers shown in Fig. 15 correspond to occultations where the receiver tracking is significantly in error within region II. The tracking results for one of these outliers are shown in Fig. 16. There exists substantial phase and frequency errors in the region where the signal amplitude is still appreciable ($50 \lesssim t \lesssim 55$). It is seen that the frequency errors in this region exceed ± 25 Hz. Thus aliasing errors will cause the tracking loop model phase to continue to wander off from the true phase even when the normal PLL mode recovers. The aliasing errors can be corrected by choosing a larger sampling bandwidth (e.g., 100 Hz instead of 50 Hz) or, in some cases, via postprocessing [*Sokolovskiy*, 2000b]. Besides the phase errors, large negative amplitude errors also result when the receiver is not tracking due to the sinc function modulation indicated in Eq. 7, although amplitude errors tend to play a more minor role than phase errors in CT processing.

The receiver tracking problems exemplified by the outliers are expected to be resolved when the PLL is replaced with open-loop tracking, where a predicted phase model is used to track the signal without any feedback [*Sokolovskiy*, 2000b]. Indeed, by fitting a simple polynomial to the relation between the bending angle and the separation angle of the transmitter and receiving satellites for a large number of occultations, it proves possible to predict the atmospheric Doppler frequency to an accuracy which is within 10 Hz [*Hajj et al.*, 2002b].

Another difference between ST and CT is that ST uses only the accumulated phase error $\Delta\phi$, while CT depends on the *wrapped* phase (i.e., phase modulo integral multiples of 2π). In other words, a phase error of $\Delta\phi = 0.5$ cycles would have the same effect on CT retrieval as $\Delta\phi = 100.5$ cycles. For this reason, we also examine the wrapped phase error defined as

$$\Delta\phi_w = \text{atan2}(\sin(\Delta\phi), \cos(\Delta\phi)) \tag{12}$$

where $\text{atan2}(y, x)$ is the four-quadrant arctangent function ($-\pi \le \Delta\phi_w \le \pi$). In Fig. 17, we show $\Delta\phi_w$ for the occultation of Fig. 13, separating the data points when FW is on and when FW is off. It is interesting to note that in region II, $\Delta\phi_w$ is clustered around 0 and $\pm\pi$. This is the case even when FW is switched off. In fact, the half-cycle errors are caused by the cycle slips (or advances) accumulated during FW. Since the residual phase is obtained by applying the two-quadrant arctangent operator (Eq. 10), there exists a half-cycle ambiguity that the receiver is unable to correct as it once again locks on to the signal. These half-cycle offsets cause the measured field to be 180° out-of-phase with respect to the true field. Serious errors can occur when CT sums up contributions from these regions together with error-free regions. To verify that most of the errors in refractivity can be eliminated by using a four-quadrant arctangent operator, we reprocess the occultation by setting the navigation data bits $D(t_i)$ to 1 and using atan2 instead of atan to extract the residual phase. The corresponding refractivity retrievals are shown in Fig. 18. The significant improvement in CT retrieval when atan2 is used in the traditional PLL was first noted by *Beyerle et al.* [2002]. It is remarkable that even the outliers are now much improved (cf. Fig. 15). The implementation of the atan2 operation in real occultation measurements requires modifications to the receiver operation to store and remove the navigation data bits from the GPS signal; this task is currently undertaken.

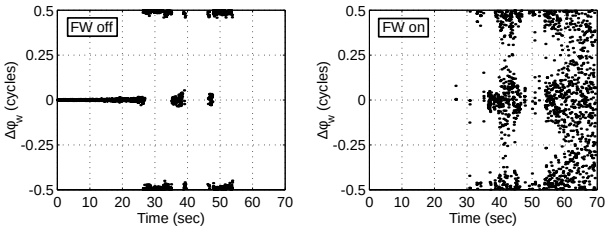

Figure 17. Wrapped phase error during periods when flywheeling is on or off.

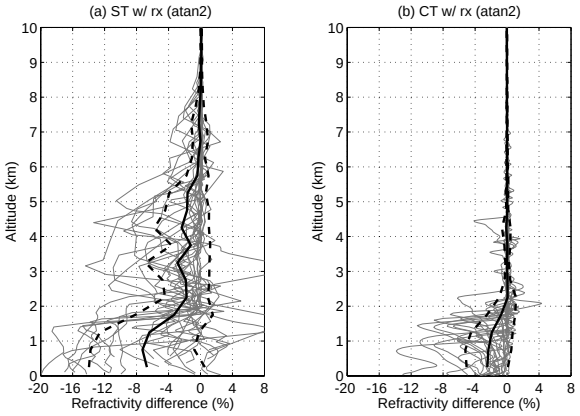

Figure 18. Same as Fig. 15 except that atan2 is used to extract the residual phase.

The simulation results presented in this section show that the current retrieval methods are sensitive to receiver tracking errors which could occur in the lower troposphere. The problems identified here are likely to be resolved in the near future with the implementation of open-loop tracking and the removal of the navigation data bits. In the meantime, lower tropospheric occultation data (especially below 2 km), should be used with caution. It is also important that the badly tracked data be properly filtered out. A robust quality control procedure can be established by comparing the observed Doppler with the predicted Doppler derived for open-loop tracking [*Hajj et al.*, 2002b; *Sokolovskiy*, 2000b] and rejecting the data when the difference is large.

6. Comparison with ECMWF

The observed N-bias shown in Sec. 2 is defined with respect to NWP models. Therefore, the comparisons with true profiles do not provide direct information on any systematic bias that might be inherent in the analyses. A limited assessment in the accuracy of ECMWF can be made by comparing the refractivity profiles from the radiosonde observations with ECMWF analyses interpolated to the times and locations of the radiosondes. Fig. 19 shows that a sizeable negative bias ($\approx 2\%$) exists in the altitude range 1–3 km, while a small positive bias exists between 3–6 km. The analysis is either missing or smoothing over the sharp features in the humidity profiles at these altitudes.

Consider next the refractivity difference when we compare the retrievals from Sec. 5 with the ECMWF profiles instead of the input radiosonde profiles (Fig. 20). As expected, there is more scatter, with larger negative bias especially in

the range of 2–3 km. A small positive bias between 3–6 km is also noticeable in the CT retrievals. This is consistent with the positive bias observed in the tropics at these altitudes as shown in Fig. 2.

How well does the N-bias obtained from the end-to-end simulations explain the N-bias from the actual occultation data? For this evaluation, we select a group of CHAMP and SAC-C occultations from October 2001. The selected occultations have tangent points with latitudes within 40°S and 55°N and longitude within 40°E and 25°E. These constraints are chosen such that the occultations are geographically close to the radiosonde sounding locations (Fig. 7), even though the times are five years apart. A total of 91 occultations are found to satisfy these criteria. Fig. 21 shows the ST and CT retrievals for these occultations. Considering the inexact nature of these comparisons, the statistical characteristics of the retrievals from the real occultations are remarkably similar to those from the simulated occultations. This is particularly true for CT retrievals and suggests that we have captured in this simulation study the main ingredients behind the observed N-bias despite the imposed simplifications.

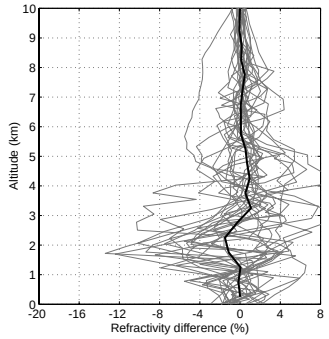

Figure 19. Fractional refractivity difference between radiosonde and ECMWF profiles $\delta N(\text{raob}, \text{ECMWF})$. Thick solid line represents the mean.

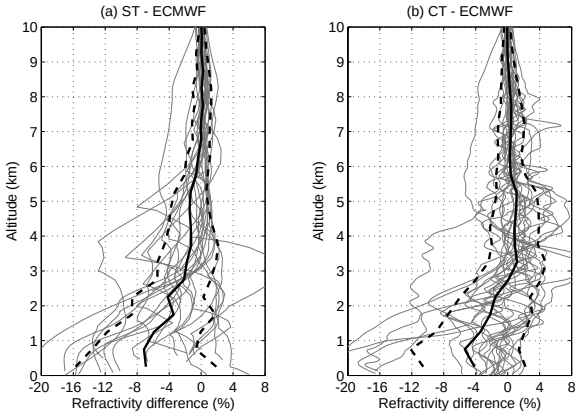

Figure 20. Fractional refractivity difference between retrieved and ECMWF profiles $\delta N(\text{occ}, \text{ECMWF})$ for simulated occultations.

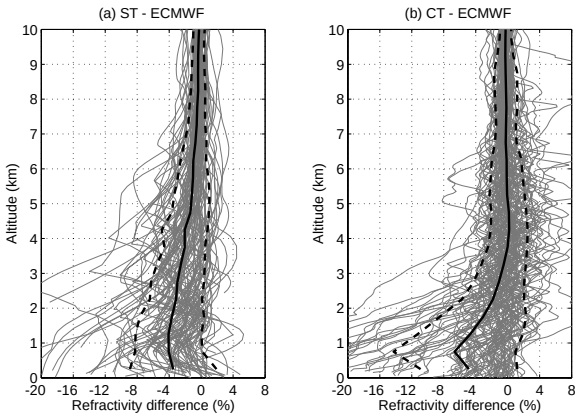

Figure 21. Fractional refractivity difference between retrieved and ECMWF profiles $\delta N(\text{occ}, \text{ECMWF})$ for CHAMP and SAC-C occultations.

7. Conclusion

Substantial progress has been made in recent years to address the challenges involved in the remote sensing of the Earth's lower troposphere by the use of GPS occultation. The development of radioholographic approaches, in particular the canonical transform method, has finally resolved the longstanding problems associated with atmospheric multipath. Implementation of the flywheeling capability in the GPS receiver tracking algorithm has allowed occultation data to be collected down to the surface of the Earth. However, as the simulation study in this paper makes clear, significant hurdles still remain to be overcome.

Similar to GPS/MET data, recent CHAMP and SAC-C refractivity retrievals are found to exhibit a negative bias with respect to numerical weather prediction models such as ECMWF in the lower troposphere (0–6 km in altitude) and predominantly over the tropics. With CT processing, the negative bias seen in the standard retrievals can be eliminated above 2 km, suggesting that atmospheric multipath is responsible for the bias there. However, the negative bias below 2 km remains and can reach -10% when averaged over one-month of data with very little quality control.

The first important question to ask about the negative N-bias is: how much, if any, of this negative N-bias can be attributed to errors in the occultation retrievals? To answer this question, we employ end-to-end simulation studies where given an input refractivity profile, a synthetic (but realistic) occultation can be generated. The synthetic data are inverted to yield the retrieved refractivity profile. Direct comparison of the retrieved refractivity with the true profile allows us to evaluate different parts of the retrieval system. An important component of an occultation simulation system is the modeling of signal tracking by the receiver. The receiver tracking errors turn out to play a significant role in the N-bias, so it is imperative that the tracking algorithm simulated closely resembles the one used aboard CHAMP and SAC-C. This is the case in the present study.

The simulations are performed using radiosonde measurements taken over the Atlantic Ocean (covering latitudes 30°S to 50°N). Based on the simulation results, we conclude that the principal cause behind the N-bias is the large refractivity gradients that are often present in the Earth's lower troposphere and are due primarily to the spatial distribution of water vapor. The large refractivity gradients not only lead to substantial receiver tracking errors, but it could also cause the Abel inversion method to fail. We summarize our main findings as follows:

1. CT retrievals constitute a great improvement over ST, in terms of accuracy and vertical resolution.

2. Ducting, often associated with the top of the planetary boundary layer at 1–2 km altitude, represents a fundamental limitation of Abel inversion that affects both CT and ST. As a result, CT refractivity retrievals are negatively biased below 2 km. For the refractivity profiles used in the simulations, the mean CT bias is at less than −1% in the absence of receiver tracking errors.

3. Most of the occultations are well-tracked by the receiver. However, they contain "half-cycle" errors due to the use of the two-quadrant arctangent operator to extract the residual phase. These errors could affect refractivity retrievals up to 8 km. The refractivity errors appear "random" (i.e., equal occurrence of positive and negative errors) above 2 km but tend to increase the negative bias below 2 km.

4. Five of the 24 simulated occultations are poorly-tracked. These cases arise when the receiver is forced to be flywheeling for an extended period of low SNR. They give maximum refractivity errors near −20% for CT. If these "outliers" are not removed, the mean N-bias for CT could increase to −4%.

5. Comparison with ECMWF (in lieu of the true profiles) increases the negative N-bias between 1–3 km. The simulated N-bias with respect to the observed N-bias from CHAMP and SAC-C in the same geographical region shows remarkable similarities, suggesting that our simulation study has captured the essential ingredients behind the observed N-bias.

With the present understanding of the N-bias, the next question that we must address is: how can the occultation retrievals be improved? Improvements in receiver tracking in the near future should help. Compensating for the navigation data bits would remove half-cycle ambiguities that are responsible for much of the CT retrieval errors. The implementation of open-loop tracking would eliminate the outliers where the FW-enhanced PLL is not capable of tracking. The problem associated with ducting, however, appears difficult to solve without the use of auxiliary information or abandoning Abel inversion altogether. The solution to this problem holds the key to using radio occultation for the remote sensing of the planetary boundary layer.

Acknowledgments. We thank R. Weller of the Alfred Wegener Institute for Polar and Marine Research, Bremerhaven, Germany, for the high-resolution radiosonde data. Helpful discussions with B. A. Iijima, E. R. Kursinski, S. S. Leroy, P. Poli, and M. de la Torre Juárez, L. E. Young, and T. P. Yunck are gratefully acknowledged. This work was carried out at the Jet Propulsion Laboratory, California Institute of Technology, under a contract with the National Aeronautics and Space Administration.

References

K. D. Anderson. Radar detection of low-altitude targets in a maritime environment. *IEEE Trans. Antennas Propagat.*, 43(6):609–613, June 1995.

C. O. Ao, G. A. Hajj, T. K. Meehan, S. S. Leroy, E. R. Kursinski, M. de la Torre Juárez, B. A. Iijima, and A. J. Mannucci. Backpropagation processing of GPS radio occultation data. In *Proceedings of the 1st CHAMP Science Meeting*, Potsdam, Germany, Jan. 2002.

B. Beyerle, M. E. Gorbunov, and C. O. Ao. Simulation studies of GPS radio occultation measurements. *Radio Sci.*, (submitted), 2002.

G. Fjeldbo, A. J. Kliore, and V. R. Eshleman. The neutral atmosphere of Venus as studied with the Mariner V radio occultation experiments. *Astron. J.*, 76:123–140, 1971.

M. E. Gorbunov. Radioholographic methods for processing radio occultation data in multipath regions. *Danish Meteorological Institute Scientific Report (Copenhagen)*, (01-02), 2001.

M. E. Gorbunov. Canonical transform method for processing radio occultation data in the lower troposphere. *Radio Sci.*, 37(5):10.1029/2000RS002592, 2002.

M. E. Gorbunov and A. S. Gurvich. Microlab-1 experiment: multipath effects in the lower troposphere. *J. Geophys. Res.*, 103(D12):13819–13826, 1998.

M. E. Gorbunov, A. S. Gurvich, and L. Kornblueh. Comparative analysis of radioholographic methods of processing radio occultation data. *Radio Sci.*, 35(4):1025–1034, 2000.

T. Hacck and S. D. Burk. Summertime marine refractivity conditions along coastal California. *J. Appl. Meteorology*, 40(4):673–687, 2001.

G. A. Hajj, C. O. Ao, B. A. Iijima, D. Kuang, E. R. Kursinski, A. J. Mannucci, T. K. Meehan, L. J. Romans, M. de la Torre Juárez, and T. P. Yunck. CHAMP and SAC-C atmospheric occultation results and intercomparisons. *J. Geophys. Res.*, submitted, 2002*a*.

G. A. Hajj, E. R. Kursinski, L. J. Romans, W. I. Bertiger, and S. S. Leroy. A technical description of atmospheric sounding by GPS occultation. *J. Atmospheric and Solar-Terrestrial Phys.*, 64(4):451–469, 2002*b*.

M. P. M. Hall. *Effects of the Troposphere on Radio Communication.* The Institution of Electrical Engineers, London, 1979.

K. Igarashi, A. Pavelyev, K. Hocke, D. Pavelyev, I. A. Kucherjavenkov, S. Matyugov, A. Zakharov, and O. I. Yakovlev. Radio holographic principle for observing natural processes in the atmosphere and retrieving meteorological parameters from radio occultation data. *Earth Planets Space*, 52:893–899, 2000.

E. R. Kursinski and G. A. Hajj. A comparison of water vapor derived from GPS occultations and global weather analyses. *J. Geophys. Res.*, 106(D1):1113–1138, 2001.

E. R. Kursinski, G. A. Hajj, J. T. Schofield, R. P. Linfield, and K. R. Hardy. Observing earth's atmosphere with radio occultation measurements using the Global Positioning System. *J. Geophys. Res.*, 102(D19):23429–23465, 1997.

M. Levy. *Parabolic Equation Methods for Electromagnetic Wave Propagation.* The Institution of Electrical Engineers, London, 2000.

J. Martin. Simulation of wave propagation in random media: theory and applications. In V. I. Tatarskii, A. Ishimaru, and V. U. Zavorotny, editors, *Wave Propagation in Random Media (Scintillation)*, pages 463–486. SPIE Press, Bellingham, 1992.

C. Rocken, R. Anthes, M. Exner, D. Hunt, S. Sokolovskiy, R. Ware, M. Gorbunov, W. Schreiner, D. Feng, B. Herman, Y.-H. Kuo, and X. Zou. Analysis and validation of GPS/MET data in the neutral atmosphere. *J. Geophys. Res.*, 102(D25):29849–29866, 1997.

E. K. Smith and S. Weintraub. The constants in the equation for atmospheric refractive index at radio frequencies. *Proc. IRE*, 41:1035–1037, 1953.

S. V. Sokolovskiy. Modeling and inverting radio occultation signals in the moist troposphere. *Radio Sci.*, 36(3):441–458, 2001*a*.

S. V. Sokolovskiy. Tracking tropospheric radio occultation signals from low Earth orbit. *Radio Sci.*, 36(3):483–498, 2001*b*.

S. V. Sokolovskiy. Effect of super refraction on inversions of radio occultation signals in the lower troposphere. *Radio Sci.*, (submitted), 2002.

J. J. Spilker Jr. GPS signal structure and theoretical performance. In B. W. Parkinson and J. J. Spilker Jr., editors, *Global Positioning System: Theory and Applications (Volume 1)*, pages 57–119. American Institute of Aeronautics and Astronautics, Washington D.C., 1996.

J. B. Thomas. *Signal-Processing Theory for the TurboRogue Receiver.* JPL Publication 95-6, 1995.

G. L. Tyler. Radio occultation experiments in the outer solar system with Voyager. *Proc. IEEE*, 75:1404–1431, 1987.

R. Ware, C. Rocken, F. Solheim, M. Exner, W. Schreiner, R. Anthes, D. Feng, B. Herman, M. Gorbunov, S. Sokolovskiy, K. Hardy, Y. Kuo, X. Zou, K. Trenberth, T. Meehan, W. Melbourne, and S. Businger. GPS sounding of the atmosphere from low Earth orbit — preliminary results. *Bull. Am. Meteorol. Soc.*, 77:19–40, 1996.

J. Wickert, C. Reigber, G. Beyerle, R. König, C. Marquardt, T. Schmidt, L. Grunwaldt, R. Galas, T. K. Meehan, W. G. Melbourne, and K. Hocke. Atmospheric sounding by GPS radio occultation: first results from CHAMP. *Geophys. Research Lett.*, 28(17):3263–3266, 2001.

T. P. Yunck, G. F. Lindal, and C. H. Liu. The role of GPS in precise earth observation. In *IEEE Position, Location and Navigation Symposium*, Orlando, FL, Nov. 29–Dec. 2, 1988.

C. O. Ao, Jet Propulsion Laboratory, M/S 238-600, 4800 Oak Grove Dr., Pasadena, CA 91109, USA. (chi.o.ao@jpl.nasa.gov)

(Received _____.)